JOURNAL OF GEOSCIENCES INSIGHTS
Jan-Mar 2026, VOL. 4, ISSUE 1, pp.1-7
https://doi.org/10.61577/jgi.2026.100001

RESEAPRO JOURNALS

ORIGINAL ARTICLE

Numerical stress fields meet machine learning: A new approach to earthquake forecasting in Western Tien Shan

Ikram Atabekov

Department of Geoinformatics and AI Laboratory, Institute of Seismology, Tashkent, Uzbekistan

ABSTRACT

Earthquake prediction in regions of complex tectonics remains a fundamental challenge in geophysics. Central Asia, and particularly Uzbekistan, is characterized by intense crustal deformation due to the interaction of the Indian, Arabian and Eurasian plates. In this study, we integrate numerical modeling of the stress–strain state of the lithosphere with advanced machine learning methods to improve seismic hazard assessment. A regional stress model at seismogenic depths (15–20 km) was developed, incorporating tectonic zoning and boundary conditions that reflect both welded and frictional fault contacts. The model reproduces the first-order distribution of stresses and velocities and shows strong agreement with independent GPS observations and focal mechanism solutions. To extend these results toward predictive applications, the outputs of the numerical model were combined with seismological and morphological features and analyzed using a hybrid Kolmogorov–Arnold Network coupled with an LSTM framework. The machine learning system successfully identified zones of elevated seismic hazard in the Western Tien Shan, which coincided with the locations of strong earthquakes that occurred in 2023. These results confirm that combining geodynamic modeling with artificial intelligence provides a powerful approach for linking stress accumulation to earthquake occurrence. The methodology offers both a robust geophysical foundation and a practical predictive tool for regions of high seismic risk.

KEY WORDS

Western Tien Shan, Stress- strain, numerical modeling, Geodynamics, Kolmogorov-Arnold network

ARTICLE HISTORY

Received 26 February 2026; Revised 17 March 2026; Accepted 28 March 2026

Introduction

Earthquake prediction remains one of the most complex and urgent problems in modern geophysics. Central Asia, and particularly Uzbekistan, is among the region's most vulnerable to seismic hazards due to its location at the boundary of several interacting lithospheric plates. Historical and instrumental records demonstrate that the territory has experienced numerous destructive earthquakes, underscoring the necessity of reliable seismic hazard assessment.

Traditional approaches, such as the Gutenberg–Richter law, focal mechanism studies, and long-term geodetic observations (e.g., GPS), have provided valuable insights into the nature of seismicity and crustal deformation. However, these methods are often limited in their ability to capture the underlying stress–strain processes within the lithosphere that control the accumulation and release of seismic energy.

In recent years, numerical modeling of the stress field at seismogenic depths has emerged as an effective tool for linking geodynamic processes with seismic hazard. Such models allow for the simulation of regional deformation patterns under specified boundary conditions, enabling direct comparison with independent observations. Nevertheless, there remains a gap between physically based models and predictive frameworks that can anticipate the time, location, and magnitude of future earthquakes.

The present study addresses this gap by integrating numerical modeling of the crustal stress–strain state with machine learning methods. Based on a geodynamic hypothesis that the deformation of Central Asia results from the combined pressure of the Indian, Arabian and Eurasian plates, we construct a regional model of stress and velocity fields at depths of 15–20 km, validated against GPS data and focal mechanism solutions.

Finally, we incorporate the outputs of the numerical model into a hybrid deep learning architecture (Kolmogorov–Arnold Network combined with LSTM), which allows us to explore spatial –magnitude patterns of seismicity and assess the potential for earthquake prediction.

Methods

Numerical experiment based on the plate interaction hypothesis

The ongoing collision of the Indian and Arabian plates with Eurasia exerts a strong northward and northwestward compressional force, while the stable Eurasian plate resists this motion from the north (Figure 1).

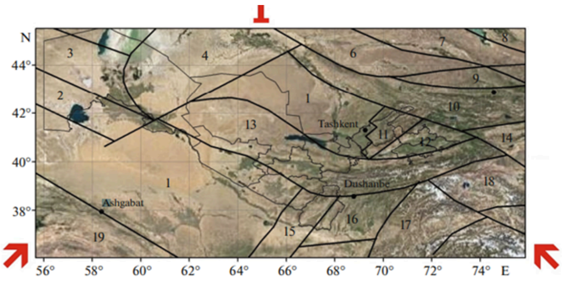

Figure 1. Collision hypothesis of the Indian and Arabian plates with Eurasia.

This triangular configuration creates a unique stress environment, leading to the intense deformation and mountain building observed across the Tien Shan and adjacent regions. To test this hypothesis, a simplified numerical experiment was carried out. The model domain was represented as an elastic

***Correspondence:** Dr. Ikram Atabekov, Department of Geoinformatics and AI Laboratory, Institute of Seismology, Tashkent, Uzbekistan, e-mail: ikramatabekov1@gmail.com

prism corresponding to the Central Asian lithosphere. Boundary conditions were prescribed to reflect the interaction of the three plates: compressional loading from the south (Indian and Arabian plates), counteracting resistance from the north (Eurasian plate). The material properties of the lithosphere were assumed to be laterally heterogeneous but zonally homogeneous within major tectonic domains. The boundaries between these zones were specified either as welded (perfect contact) or as frictional fault interfaces. This allowed us to compare two end-member scenarios: full cohesion across the boundary and partial slip governed by Coulomb-type friction. The inverse problem of geomorphogenesis is a numerical experiment for boundary conditions: we do not set them manually but find conditions under which a flat lithosphere is deformed into a real relief (Figure 2) [1]. At each stage of the experiment, internal stresses were compared with the absolute value of the greatest shear stresses at a depth of 10-20 km based on tectonic movements over the past 30 million years and seismicity over 50 years obtained in [2].

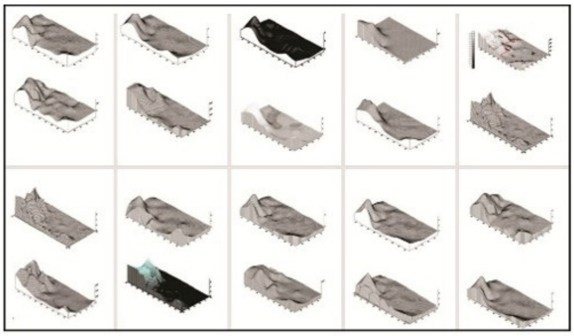

Figure 2. A few samples of numerical experiments for boundary conditions under which a flat lithosphere is deformed into real relief. The First picture is built on the base of modern relief; the last is the result of an experiment.

Despite the simplified geometry, the experiment reproduced the first-order pattern of crustal deformation, including the north–south shortening across the Tien Shan and the rotation of the Fergana Basin. These results provide evidence that the deformation of Central Asia can be interpreted as a direct consequence of the combined pressure of the three surrounding plates.

Modelling of modern movements of Earth's crust in Central Asia

The preliminary experiment serves as the physical basis for modeling modern movements of Central Asia by Stockes equations, where present-day motions are reconstructed using initial internal elastic stresses. The average Stokes equations applied to depths of the earth's crust of 15-20 km for horizontal displacement (x_1, x_2) and pressure (x_1, x_2) have the following form [3]:

$$-grad\,\overline{p} + \mu\Delta\overline{v} = F \quad (1)$$

$$\overline{divv} = 0 \quad (2)$$

where F (F_1, F_2) is a vector with components

$$F_1 = \frac{(1-k_z)}{(h-H)}\overline{\sigma_{11}}\frac{\partial H}{\partial x_1} + \frac{(1-k_z)}{(h-H)}\overline{\sigma_{12}}\frac{\partial H}{\partial x_2} - \frac{\partial}{\partial x_1}\left(\frac{(1-k_z)}{(h-H)}\frac{\partial H}{\partial x_1}\overline{v_1}\right) - \frac{\partial}{\partial x_2}\left[\frac{2(1-k_z)}{(h-H)}\frac{\mu}{\mu_0}\left(\frac{\partial H}{\partial x_2}\overline{v_1} + \frac{\partial H}{\partial x_1}\overline{v_2}\right)\right] - \frac{1}{(h-H)}\left[v_3(x_1,x_2,H)\frac{\partial H}{\partial x_1} + \frac{\partial v_3(x_1,x_2,H)}{\partial x_1}\right)], \quad (3)$$

$$F_2 = \frac{1}{2(h-H)}\overline{\sigma_{21}}\frac{\partial H}{\partial x_1} + \frac{1}{2(h-H)}\overline{\sigma_{22}}\frac{\partial H}{\partial x_2} - \frac{\partial}{\partial x_1}\left[\frac{2(1-k_z)}{(h-H)}\frac{\mu}{\mu_0}\left(\frac{\partial H}{\partial x_2}\overline{v_1} + \frac{\partial H}{\partial x_1}\overline{v_2}\right)\right] - \frac{\partial}{\partial x_2}\left(\frac{(1-k_z)}{(h-H)}\frac{\partial H}{\partial x_2}\overline{v_2}\right) - \frac{1}{(h-H)}\left[v_3(x_1,x_2,H)\frac{\partial H}{\partial x_2} + \frac{\partial v_3(x_1,x_2,H)}{\partial x_2}\right)] \quad (4)$$

In these formulas, σ_{ij} with a bar is the initial stress reconstructed in (1), H (x_1, x_2)is the topography of the Earth's surface, h=const is the depth of the lithosphere, ρ is the density, μ is the viscosity coefficient, and Δ is the two-dimensional Laplace operator. k_z is the coefficient which appears in averaging [1,3]. The functions as w (x_1, x_2, x_3) were averaged by the following formula:

$$\overline{w}(x_1, x_2) = \frac{1}{(h-H)}\int_H^h w(x_1, x_2, x_3)dx_3 \quad (5)$$

The derivation of equations for the average velocity of movement (1–4) is carried out considering the Leibniz formula for integrals whose integration limits depend on (x_1, x_2). For example,

$$\frac{\partial\overline{\sigma_{ij}}}{\partial x_k} = \frac{\partial}{\partial x_k}\left(\frac{1}{h-H}\int_H^h \sigma_{ij}dx_3\right) = \frac{1}{(h-H)^2}\int_H^h \sigma_{ij}dx_3 + \frac{1}{h-H}\int_H^h \frac{\partial\sigma_{ij}}{\partial x_k}dx_3 + \frac{1}{(h-H)}\sigma_{ij}\Big|_{x_3=h}\frac{\partial h}{\partial x_k} - \frac{1}{(h-H)}\sigma_{ij}\Big|_{x_3=H}\frac{\partial H}{\partial x_k}) = \overline{\frac{\partial\sigma_{ij}}{\partial x_k}} + \frac{\sigma_{ij}(x_1,x_2,h)}{(h-H)}\frac{\partial h}{\partial x_k} + \frac{(\overline{\sigma_{ij}} - \sigma_{ij}(x_1,x_2,H)}{(h-H)}\frac{\partial H}{\partial x_k} \quad (6)$$

When deriving equations, the relationships that follow from the accepted averaging rule are also used:

$$\overline{\sigma}_{33} = \frac{1}{2}(\sigma_{33}|_h + \sigma_{33}|_H) = \frac{1}{2}\sigma_{33}|_h = \frac{1}{2}\frac{\rho g(h-H)}{\mu/t_0} \quad (7)$$

$$\overline{\sigma}_{i3} = \frac{1}{2}(\sigma_{i3}|_h + \sigma_{i3}|_H) = \frac{1}{2}k_a\frac{\rho g(h-H)}{\mu/t_0}$$

For i=1,2. k_a is the friction coefficient on the lithosphere.

The vertical velocity of displacements on the Earth's surface is obtained by averaging of the incompressibility equation (2), assuming v_3(x_1, x_2, h) = 0:

$$v_3(x_1,x_2,H) = (h-H)\left(\frac{\partial\overline{v_1}}{\partial x_1} + \frac{\partial\overline{v_2}}{\partial x_2}\right) - (1-k_z)\left(\frac{\partial H}{\partial x_1}\overline{v_1} + \frac{\partial H}{\partial x_2}\overline{v_2}\right) \quad (9)$$

The equations (1-4) were solved by the boundary element method. The obtained velocity fields were identified by GPS data [4] (Figure 3).

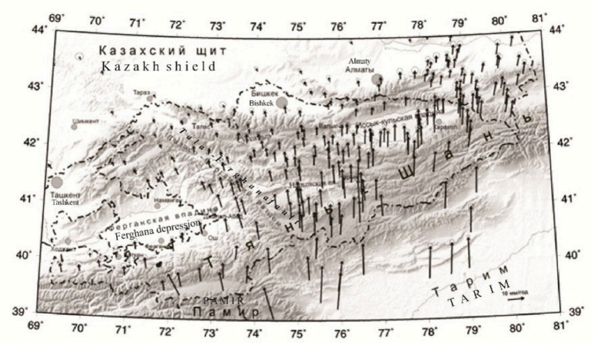

Figure 3. Recent horizontal velocity pattern of the Tien Shan fragment of the Central Asian GPS network, as calculated relative to stable parts of the Eurasian plate [4].

Modelling of modern movements of Earth's crust in Central Uzbekistan

While the simplified plate interaction experiment provides a first-order explanation of the deformation framework in Central Asia, it does not capture the complexity of present-day motions and stress accumulation. Within this context, Uzbekistan plays a key role, and therefore we performed a

https://doi.org/10.61577/jgi.2026.100001

more detailed analysis of stress conditions in its territory (Figure 4).

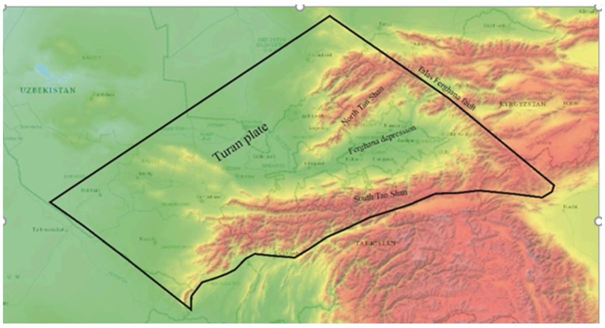

Figure 4. The territory under consideration for constructing mathematical model of stress.

The external boundary conditions of the model were constrained using geodetic data, primarily GPS velocities, representing crustal motions over the last 20–25 years. Topographic variations and zonal differences in density and rheology were included to improve the realism of the regional stress field. We chose z=8-10 km corresponding to the basement depth in the Fergana Depression, since the prevailing GPS data are available for this part of Uzbekistan. The velocities in the boundary conditions of the mathematical problem were taken equal to the velocities from works [4] (Figure 2), if possible, at those points where data are available. In the Southern Tien Shan, the velocities relative to Eurasia are directed northwest with values of 10-15 mm/year. Along the Talas-Fergana fault, the tangential velocities are directed along the fault at a value of 5-10 mm/year, gradually decreasing to the northern boundaries in the north to 1-2 mm/year. In this case, the normal to the boundary velocities remained constant 2-3 mm/year. To validate the numerical results, we compared the modeled velocities and orientations of the maximum horizontal stress axis (σ_1) with published data from focal mechanism solutions and independent stress compilations.

Machine learning framework

The outputs of the geodynamic model (stress components, velocity fields, and strain parameters) were combined with classical seismological and morphological features to form the input dataset for machine learning. The basis of machine learning for earthquake prediction is a dataset with predictive features. A neural network, trained on this data, primarily using statistical methods, can find a relationship between earthquake probabilities. The novelty of the Kolmogorov-Arnold Network (KAN) [5-7], in contrast to conventional NPL (where constant weights are optimized), lies in finding this connection with a nonlinear function f of n variables by approximating G_k, $g_{k,i}$, representing functions of a single variable [8]. Mathematically, this is expressed as follows:

$$f(x_1, x_2, \ldots x_n) = \sum_{k=0}^{2n} G_k\left(\sum_{i=0}^{n} g_{k,i}(x_i)\right) \qquad (10)$$

Since the Kolmogorov-Arnold function approximation theorem implemented in machine learning, many hybrid architectures consisting of KANs coupled with regressive networks such as long short-term memory (LSTM) networks and convolutional neural networks (CNNs) have been implemented. This design allowed the model to capture both nonlinear feature interactions and temporal sequences of seismic activity applications of Kolmogorov-Arnold networks (KANs) have emerged in various fields of science [9,10].

The machine learning system was trained on a comprehensive earthquake catalog covering the historical to instrumental periods. Training was performed on sliding temporal windows, with the goal of predicting both earthquake magnitudes and probabilities in specific spatial zones. The model was calibrated and validated against independent subsets of the data, including the events of 2023, which provided an opportunity to test its predictive performance.

Results

Regional stress and velocity fields

The normalized vector field of displacement velocity is shown in Figure 5. Some sharp spikes in the values of the velocity vector of movement are due to the error of the numerical method at the boundary points of contact of zones with different physical parameters. The numerical model results were validated using data from several independent authors. Statistical evaluations showed that in more than 70% of cases, the angular difference was within 20°, and in nearly 40% of the cases, within 10°. This demonstrates that the model successfully captures the first-order features of the stress field.

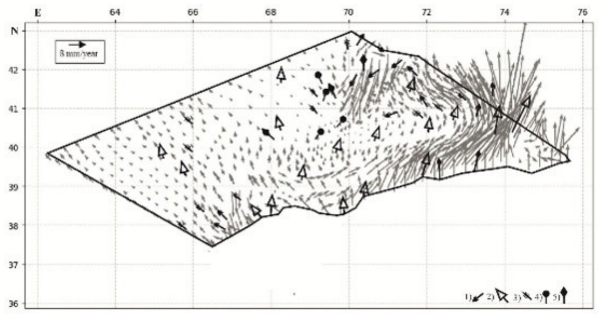

Figure 5. The velocity field obtained by the computational experiment of the stress state of the Western Tien Shan identified by data of several independent authors: 1)- [4]; 2)- [11, 12]; 3)- [13]; 4)- [14]; 5)- [15]

The vertical velocity on the Earth's surface, v_3, is calculated using formula 10 (Figure 6).

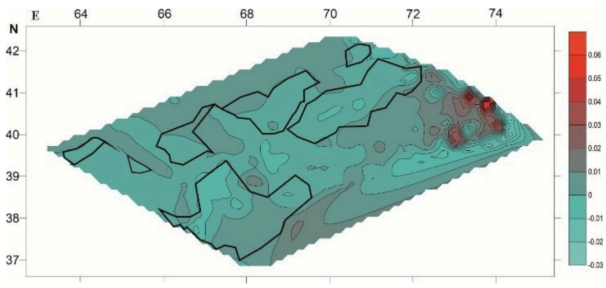

Figure 6. Vertical velocity (m/yr) on the Earth's surface based on the results of the numerical model (colour picture). Thick closed lines contain modern downward movements according to geodetic data [16].

For analyzing geodynamical state of the region, we add lithostatic pressure as σ_{33} and assume $\sigma_{13} = \sigma_{23} = k_a\sigma_{33}$. According to Byerlee's law, the frictional sliding coefficient in the Earth's crust, ka, has been chosen in a range of 0.6–1.0. The tangential stress τ (Figure 7) is obtained by the formula:

$$\tau = \frac{1}{3}\sqrt{(\sigma_{11}-\sigma_{22})^2 + (\sigma_{22}-\sigma_{33})^2 + (\sigma_{33}-\sigma_{11})^2 + 6(\sigma_{12}^2 + \sigma_{23}^2 + \sigma_{31}^2)} \qquad (11)$$

https://doi.org/10.61577/jgi.2026.100001

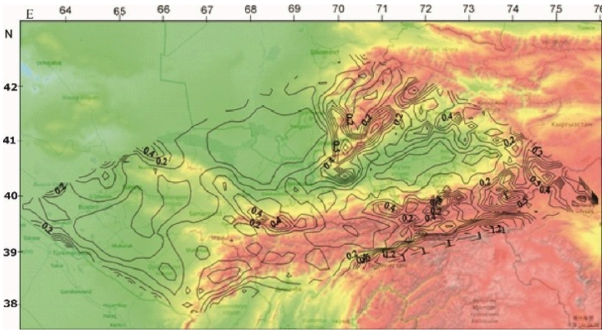

Figure 7. Tangential stresses (kbars) at depths of 15 km of the earth's crust in the Western Tien Shan.

The stress state of a continuous medium is generally determined by three principal stress vectors (conventionally $\sigma_1>\sigma_2>\sigma_3$). Their values and directions are obtained from the equation:

$$\det\left\|\sigma_{ij}-\sigma\delta_{ij}\right\|=0 \quad i, j=1, 2, 3. \tag{12}$$

For the symmetric stress tensor σ_{ij}, equation (12) always has three valid roots.

They are expressed through three invariants J_1, J_2, J_3 of the stress tensor by the formulas:

$$\sigma_1=J_1+\frac{2\sqrt{2}}{\sqrt{3}}\sqrt{J_2}\sin(\vartheta+\frac{2\pi}{3}), \tag{13}$$

$$\sigma_2=J_1+\frac{2\sqrt{2}}{\sqrt{3}}\sqrt{J_2}\sin(\vartheta), \tag{14}$$

$$\sigma_3=J_1+\frac{2\sqrt{2}}{\sqrt{3}}\sqrt{J_2}\sin(\vartheta-\frac{2\pi}{3}), \tag{15}$$

$$J_1=\frac{1}{3}\sum_{i=1}^{3}\sigma_{ii}, \tag{16}$$

$$J_2=\frac{1}{3}\sum_{i=1}^{3}\sum_{j=1}^{3}\sigma_{ij}\sigma_{ij}, \quad (17) \tag{17}$$

$$J_2=\frac{1}{3}\sum_{i=1}^{3}\sum_{j=1}^{3}\sum_{k=1}^{3}\sigma_{ij}\sigma_{jk}\sigma_{ki}, \tag{18}$$

$$\vartheta=\frac{1}{3}\arcsin(\frac{3\sqrt{3}}{2}\frac{\sqrt{J_3}}{J_2^{3/2}}). \tag{19}$$

The orientation of the vectors σ_1, σ_2, σ_3 are obtained by the next system of equations:

$$\sigma_{ij}n_i-\sigma n_j=0 \tag{20}$$

i=1,2,3 on condition

$$n_1^2+n_2^2+n_3^2=1 \tag{21}$$

The orientations of the main vector σ_1 are shown in Figure 8.

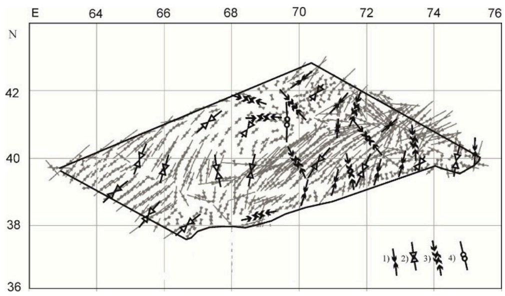

Figure 8. Orientation of main vector identified by data of several independent authors: 1)- [4]; 2)-[11, 12] ; 3)-[16]; 4)- [17].

The orientations of the σ_1 vectors from the model were compared with focal mechanism solutions published by various authors. Statistical evaluation showed that the model successfully captures the first-order features of the stress field.

Based on Anderson's method, a map of the geodynamic regime of the territory was constructed. (Figure 9).

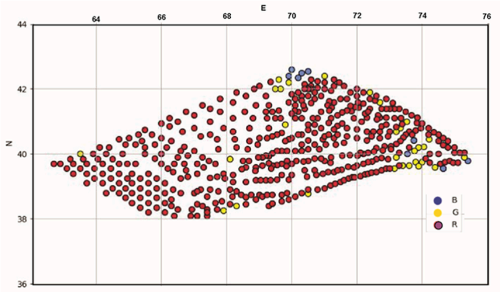

Figure 9. The geodynamic regime of the Western Tien Shan: B- normal faults, G- strike-slip faults, R- reverse faults.

The geodynamic state was compared with data obtained from earthquake focal mechanisms. Calculations based on the seismological database at all depths based on earthquakes since 1946 show that, out of a total of 450 mechanisms, 25 are strike-slip faults, 104 are normal faults, and the remaining are reverse faults.

The energy criterion is another widely used method for determining when a material loses strength. According to this criterion, the material's strength is compromised when specific energy-related conditions are violated. The context of the energy criterion, when the material is under tension, loses strength when the stored energy exceeds a critical threshold specific to tensile conditions. These conditions vary depending on whether the material is under compression or tension:

a) In compression (p<0)

$$(\sigma_1-\sigma_2)^2+(\sigma_2-\sigma_3)^2+(\sigma_3-\sigma_1)^2\leq 2{\sigma_0}^2 \tag{22}$$

b) In tensile (p>0):

$${\sigma_1}^2+{\sigma_2}^2+{\sigma_3}^2-2\nu(\sigma_1\sigma_2+\sigma_2\sigma_3+\sigma_3\sigma_1)\leq{\sigma_0}^2 \tag{23}$$

Figure 10 illustrates the locations of the Western Tien Shan region that meet the conditions (22, 23) for material failure under compression and tension, as described by the energy criterion. These zones are marked with triangles. Additionally, earthquake epicentres with a magnitude of M≥5.5 that have occurred since historical times are indicated by circles. They approximately coincide with the earthquake centres indicated by circles. Blue squares are obtained at 0.95 $\sigma_0$and correspond to locations where small stress increases can lead to earthquakes.

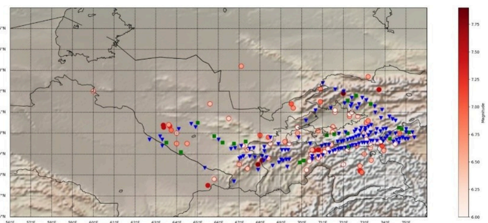

Figure 10. Locations where stresses exceed the crustal strength (triangles) and foci of earthquakes with magnitude M≥6 occurring since historical times (circles). Green squares correspond to a strength condition of 0.95 σ_0.

https://doi.org/10.61577/jgi.2026.100001

The introduction of frictional conditions on faults, as opposed to welded contacts, resulted in an increase in tangential stresses and velocities along fault zones. This effect was particularly noticeable at fault tips, where stress concentrations are expected. These differences illustrate the importance of explicitly considering fault mechanics in stress modeling.

Machine-learning predictions

The machine-learning framework, trained on the combined dataset of seismological, geodynamic, and morphological features, demonstrated the ability to predict the location and magnitude of future earthquakes.

The machine learning features included the results of mathematical modeling of the stress state of the Western Tien Shan crust, the tectonic and morphometric parameters of the region, and the seismological earthquake database:
Data determined from the seismological database:

- Year;
- Latitude;
- Longitude;
- Earthquake magnitude;
- Depth;
- Zone number;
- Difference in the Richter-Gutenberg coefficient from the mean value of the corresponding subregion (if $\Delta b \geq 0$, then 1, otherwise 0);
- Difference in the relative earthquake activity from the mean value of the territory (if $A_{10} \geq 0$, then 1, otherwise 0);
- Presence of a "seismic quiescence" zone, obtained using DBSCAN clustering and analysis of local time gaps in activity;

Terrain morphological data:

- Distance R to the nearest mountainous area: $R \leq 30$ km;
- $30 < R \leq 70$;
- $R > 70$.
- Mountains with foothills;
- Mountains with piedmont plains;
- High mountains;
- Foothills with foothills.
- Relief height h, km.

Number of faults n:

- $1 \leq n \leq 2$;
- $n > 2$.
- Fault intersection.

Length of the main fault L:

- $L \leq 300$ km;
- $300 < L \leq 700$ km;
- $L > 700$ km.
- Data obtained from the numerical model:
- Tangential stress.
- Zones where the ultimate strength exceeds σ_0.
- Horizontal velocity v_N;
- Horizontal velocity v_E;
- Vertical velocity at the Earth's surface.

Geodynamic nature of stress states according to the numerical model:

- Regional compression;
- Regional extension.

Earthquake mechanisms are constructed using the numerical model and verified by instrumental data:

- Normal fault;
- Reverse fault;
- Strike-slip fault.

The hybrid KAN+LSTM model was tested on the independent events from 2023 (Figures 11 and 12). Remarkably, the model forecasts highlighted zones of elevated seismic hazard in the Western Tien Shan, which coincided with the locations of strong earthquakes with magnitude $M < 5.2$ that occurred in 2023. In the area under consideration, all earthquakes except one had magnitudes less than $M = 5.2$. The predicted magnitudes were also consistent with the observed values, confirming the practical potential of combining numerical stress modeling with artificial intelligence.

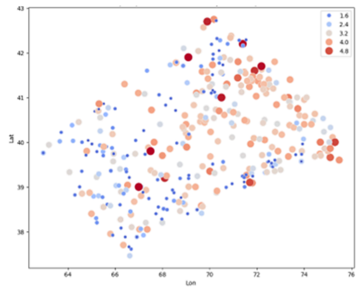

Figure 11. Predicted locations by the combined regression and classification model (KAN + LSTM) for 2023. Accuracy of geographic coordinates predicted events (with magnitude $3.9 < M < 5.2$) is $\Delta L = \pm 0.1°$.

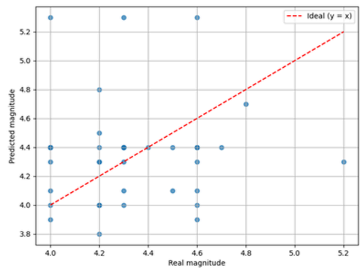

Figure 12. Magnitudes discrepancy between actual and predicted earthquakes. A y=x match is considered ideal. Accuracy of predicted magnitudes ($3.9 < M < 5.2$) is $\Delta M = \pm 0.4$.

The earthquake forecast for the future, considering events up to December 31, 2024, is in Pritashkent Region, shown in Figure 13.

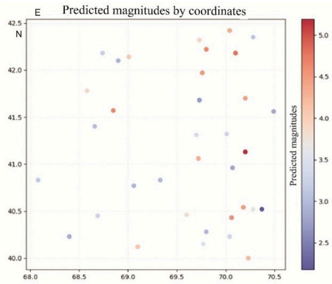

Figure 13. The earthquake forecast for the future.

https://doi.org/10.61577/jgi.2026.100001

Discussion

The present study demonstrates that integrating regional-scale stress modeling with machine learning techniques can effectively reproduce and anticipate seismic patterns in Western Tien Shan. The agreement between modeled and observed stress orientations indicates that the large-scale geodynamic framework is well captured by the numerical model. This provides confidence that the derived stress fields are suitable for assessing long-term tectonic loading and for serving as input to predictive algorithms.

The differences observed between modeled and measured data can be explained by several factors. First, the model averages stresses at depths of 15–20 km, whereas focal mechanism solutions may reflect more localized or shallower conditions. Second, GPS velocities are smoothed over 20–25 years, which suppresses short-term, fault-specific displacements. Third, the simplified representation of fault friction and contact conditions may not fully capture the complexity of fault-zone rheology and stress transfer at smaller scales.

Nonetheless, the ability of the hybrid KAN+LSTM model to highlight zones of elevated seismic hazard before the occurrence of strong earthquakes in 2023 underscores the practical significance of the approach. By combining physically based stress modeling with data-driven learning, it becomes possible to bridge the gap between geodynamic processes and probabilistic earthquake forecasting.

An important implication is that the Western Tien Shan may accumulate and release stress in distinct ways. Identifying segments of faults that exhibit stress concentration under regional loading conditions could improve seismic hazard assessment and contribute to prioritizing areas for detailed field investigations and monitoring.

Future work should focus on increasing the spatial resolution of the stress model, explicitly incorporating major fault geometries and nonlinear fault mechanics, and extending the machine learning framework with additional high-resolution geodetic and geological data. These enhancements will help to capture fine-scale variations in stress accumulation and further improve the predictive capability of the combined approach.

Of course, earthquake forecasting is inherently uncertain. Our model does not predict exact timing, but it helps narrow down where future earthquakes are more likely to occur. With further refinement and integration of real-time data, we believe this approach can contribute to early warning systems and disaster preparedness.

Conclusion

This study presents a novel framework that combines regional stress–strain modeling with machine learning to analyze and predict seismicity in Central Asia. The numerical model at 15–20 km depth reproduced the large-scale deformation patterns driven by the interaction of the Indian, Arabian, and Eurasian plates, and showed strong consistency with GPS velocities and focal mechanism data.

The integration of these physically based results with a hybrid Kolmogorov–Arnold Network and LSTM architecture enabled probabilistic forecasts of earthquake occurrence. Importantly, the model highlighted high-risk zones in the Western Tien Shan prior to the strong earthquakes of 2023, demonstrating both scientific validity and practical value.

These findings underscore that the combination of geodynamic modeling and artificial intelligence can significantly improve the reliability of earthquake forecasting. The approach establishes a solid foundation for future studies focused on fault-scale processes, rheological heterogeneities, and regional seismic hazard assessment, with direct implications for risk reduction in Uzbekistan and the wider Central Asian region.

Funding

The study was supported by funding from the Fund for Support of Seismology, Seismic Strength of Structures and Seismic Safety under the Cabinet of Ministers of the Republic of Uzbekistan.

References

1. Atabekov I. Earth Core's stresses variation in Central Asian earthquakes region. Geod. Geodyn. 2020;11(4):293-299. https://doi.org/10.1016/j.geog.2019.12.005
2. Gzovsky MV. Fundamentals of Tectonophysics. 1975. 536p.
3. Atabekov IU. Experience of modeling the seismotectonic flow of the Earth's crust in Central Asia. Izv Russ Acad Sci, Phys Solid Earth. 2021;57(1):110-119. https://doi.org/10.1134/S1069351321010018
4. Zubovich AV, Mukhamediev SA. A method of superimposed triangulations for calculation of velocity gradient of horizontal movements: application to the Central Asian GPS network. Geodyn Tectonophys. 2015;1(2):169-185. https://doi.org/10.5800/GT-2010-1-2-0013
5. Liu Z, Wang Y, Vaidya S, Ruehle F, Halverson J, Soljačić M, et al. KAN: Kolmogorov-arnold networks. arXiv preprint arXiv:2404.19756. 2024. https://doi.org/10.48550/arXiv.2404.19756
6. Xu K, Chen L, Wang S. Kolmogorov-arnold networks for time series: Bridging predictive power and interpretability. arXiv preprint arXiv:2406.02496. 2024. https://doi.org/10.48550/arXiv.2406.02496
7. Boura T, Konstantopoulos S. Seqkan: Sequence processing with kolmogorov-arnold networks. arXiv preprint arXiv:2502.14681. 2025. https://doi.org/10.48550/arXiv.2502.14681
8. Kolmogorov AN. On the representation of continuous functions of several variables by superpositions of continuous functions of a smaller number of variables. American Mathematical Society; 1961.
9. Liu Z, Wang Y, Vaidya S, Ruehle F, Halverson J, Soljačić M, Hou TY, Tegmark M. Kan: Kolmogorov-arnold networks. arXiv preprint arXiv:2404.19756. 2024. https://doi.org/10.48550/arXiv.2404.19756
10. Atabekov IU, Atabekov AI. Application of Neural Network Technologies for Tectonic Earthquake Prediction. Geotectonics. 2024;58(4):442-448. https://doi.org/10.1134/S0016852124700316
11. Zheng G, Wang H, Wright TJ, Lou Y, Zhang R, Zhang W, et al. Crustal deformation in the India-Eurasia collision zone from 25 years of GPS measurements. J Geophys Res Solid Earth. 2017;122(11):9290-9312. https://doi.org/10.1002/2017JB014465
12. Wang M, Shen ZK. Present-day crustal deformation of continental China derived from GPS and its tectonic implications. J Geophys Res Solid Earth. 2020;125(2):e2019JB018774. https://doi.org/10.1029/2019JB018774

https://doi.org/10.61577/jgi.2026.100001

13. Alimukhamedov IM, Shukurov ZF, Zubovich AV, Mohadjer S, Mosienko OI, Radjabov SS, et al. GPS measurements of Present-day Crustal Movements in Uzbekistan. Tectonics. 2025 (in print).
14. Fazilova D, Makhmudov M, Khalimov B. The analysis of crustal deformation patterns in the Tashkent region, Uzbekistan, derived from GNSS data over the period 2018–2023. Geod Geodyn. 2025;16(2):137-146. https://doi.org/10.1016/j.geog.2024.07.001
15. Shayakubov TS, Dalimov TN. Geology and Minerals of the Republic of Uzbekistan. National University of Uzbekistan, Tashkent. 1998.
16. Ibragimova TL, Ibragimov RS, Mirzaev MA, Rebetsky YL. The current stress of earth's crust in the territory of Uzbekistan according to focal earthquake mechanisms. Geodyn Tectonophys. 2021;12(3):435-454. https://doi.org/10.5800/GT-2021-12-3-0532
17. Heidbach O, Rajabi M, Cui X, Fuchs K, Müller B, Reinecker J, et al. The World Stress Map database release 2016: Crustal stress pattern across scales. Tectonophy. 2018;744:484-498. https://doi.org/10.1016/j.tecto.2018.07.007

https://doi.org/10.61577/jgi.2026.100001